Letter Vol. 48, No. 24 / 15 December 2023 / Optics Letters 6573

Ultraviolet sensing based on an in-fiber ZnO microwire constructed Mach–Zehnder interferometer

Chen Chen,[1,2] Ying Wang,[1,2,*] Han Liu,[1,2] Yubin Deng,[1,2] Xun Wu,[1,2] Changrui Liao,[1,2] Xiaoyu Weng,[2] Liwei Liu,[2] Junle Qu,[2] and Yiping Wang[1,2]

[1]Shenzhen Key Laboratory of Photonic Devices and Sensing Systems for Internet of Things, Guangdong and Hong Kong Joint Research Centre for Optical Fibre Sensors, State Key Laboratory of Radio Frequency Heterogeneous Integration, Shenzhen University, Shenzhen 518060, China
[2]Shenzhen Key Laboratory of Ultrafast Laser Micro/Nano Manufacturing, Key Laboratory of Optoelectronic Devices and Systems of Ministry of Education/Guangdong Province, College of Physics and Optoelectronic Engineering, Shenzhen University, Shenzhen 518060, China
*yingwang@szu.edu.cn

Received 28 September 2023; revised 8 November 2023; accepted 9 November 2023; posted 9 November 2023; published 14 December 2023

We propose a Mach–Zehnder interferometer based on an in-fiber ZnO microwire structure for ultraviolet sensing. The device undergoes femtosecond laser micromachining and chemical etching on a single-mode optical fiber initially, creating a microgroove that extends to half of the core's depth, into which a single ZnO microwire is transferred. The ZnO microwire and the remaining core are used as the sensing arm and the reference arm, respectively, forming a Mach–Zehnder interferometer. To enhance the stability and the sensitivity, ZnO nanoparticles are filled into the microgroove after the ZnO microwire is transferred. The fabricated device exhibits a sensitivity of 0.86 nm/(W·cm^{-2}) for ultraviolet sensing, along with a response time of 115 ns (rise time) and 133 μs (decay time), respectively. The proposed sensor exhibits good ultraviolet sensitivity, offering a novel approach for ultraviolet sensing technology.

https://doi.org/10.1364/OL.506796

The widespread utilization of ultraviolet (UV) in diverse fields, including optical communication [1], healthcare [2], military [3], environmental science [4], and astronomy [5], highlights the increasing importance of high-precision UV sensing technology. To meet the UV sensing requirements in different application environments, UV sensors based on various mechanisms have been developed, including a photomultiplier tube, a gaseous sensor, a semiconductor detector, and a fiber-optic sensor [6]. Photomultiplier tubes are renowned for their ultrahigh sensitivity and low noise [7], while gaseous sensors effectively detect high-power UV radiation [8]. However, both types suffer from drawbacks in terms of their large size and high power consumption, limiting their applicability in miniaturized devices. Solid-state UV photodetectors (based on Si or wide bandgap semiconductors) exhibit unique wavelength-selective responses and facile integration into circuits [9]. Nevertheless, they still encounter challenges associated with dark currents and slow response times. In recent years, fiber-optic sensors have emerged as a focal point of research in the sensor field due to their compact size, cost-effectiveness, immunity to electromagnetic interference, and flexible measurement positions [10]. Because the optical fiber material (SiO_2) itself exhibits insensitivity to UV, it is often necessary to integrate specific functional materials with the fiber to achieve UV sensing. Presently, a diverse array of materials finds application in UV sensing, such as semiconductor materials like SiC [11], $AlGaN$ [12], Ga_2O_3 [13], and ZnO [14], as well as polymers like $La_2O_2S:Eu^{3+}$ [15] and phosphorus-doped epoxy resins [16].

Among them, zinc oxide (ZnO), as a classic direct wide bandgap (3.37 eV) semiconductor, has become an ideal candidate for UV sensing due to its large exciton binding energy, good infrared transparency, excellent UV absorption, and simple fabrication process [17]. In particular, low-dimensional ZnO micro/nanomaterials possess a large surface area and deep-level surface trap states, which effectively enhance the carrier lifetime, and the dimensional reduction of the active region shortens the carrier transport time. Consequently, it exhibits high photosensitivity, thus better stimulating the sensing and responsive performance of the sensor [18]. In 2002, Yang *et al.* [19] utilized a single ZnO nanowire for UV sensing, and its excellent UV responsiveness and miniaturization inspired numerous researchers to focus on UV sensors based on ZnO micro/nano materials [20,21]. In 2019, Zhang *et al.* [22] proposed an all-fiber coupler that utilized ZnO nanowire directly coupled to a microfiber through van der Waals force. This innovative design enabled the efficient sensing of UV while eliminating electromagnetic interference. In 2020, Shen *et al.* [23] applied a ZnO–graphene composite coating to the surface of a single-mode-tapered multi-mode–single-mode fiber structure, resulting in a highly precise and sensitive all-fiber UV sensor. Despite some advancements in fiber-based UV sensing technology, challenges such as structural instability and low sensitivity still exist.

In this Letter, a compact fiber-optic UV sensor based on a Mach–Zehnder interferometer (MZI) structure is proposed. In this sensor, a single-mode fiber (SMF) is processed through femtosecond laser micromachining and chemical etching to create a microgroove, whose depth reaches half of the core.

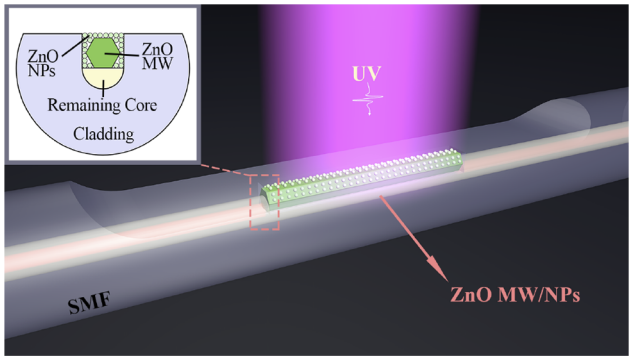

Fig. 1. 3D diagram of the proposed UV sensor based on a fiber-optic MZI, where the top-left inset provides the cross section of the sensing area.

The microgroove is then filled with a single ZnO microwire (MW)/nanoparticles (NPs), acting as the sensing arm for the MZI. The remaining half of the core functions as the reference arm. Under the influence of UV, a large amount of photocarriers is generated in the ZnO, causing a transient effective refractive index (RI) change and resulting in a redshift (drift toward a longer wavelength) in the interference wavelength. The UV intensity can be determined by tracing the wavelength shift. The proposed device achieves a sensitivity of 0.86 nm/(W·cm^{-2}) when illuminated by 257-nm UV light. It exhibits excellent responsiveness with rise time and decay time of 115 ns and 133 μs, respectively.

Figure 1 illustrates the 3D diagram of the proposed MZI-based fiber-optic UV sensor, of which the cross-sectional view is inset on the top left. For the consideration of better size matching and simple two-beam interference, SMF (8/125 μm) is chosen as the base of the sensor. The optical signal is transmitted through the core of SMF to the sensing area, where it is bifurcate into two optical paths: one directs toward ZnO MW and the other toward the core. At the output end face, the two paths recombine to form an interference, whose free spectral range depends on the length of the ZnO MW. When exposed to UV illumination, the generation of photocarriers causes an RI increase of the ZnO material. Because the presence of carriers in semiconductors can lead to change in the absorption coefficient through the competitive energy band filling effect and bandgap shrinkage effect, which, in turn, induces considerable alterations in the RI of semiconductors, as can be predicted by the Kramers–Kronig relationship [24]:

$$\Delta n(N,P,E) = \frac{2c\hbar}{e^2} P \int_0^{\infty} \frac{\Delta\alpha(N,P,E')}{E'^2 - E^2}\, dE', \tag{1}$$

where N and P are the concentrations of free electrons and holes, respectively. The terms E, c, $\hbar$, e, and $\Delta\alpha$ are the photon energy, the speed of light, Planck's constant, the electron charge, and the change in the absorption coefficient, respectively, and $P\int$ indicates the principal value of the integral. The absorption coefficient of ZnO will increase in the case of relatively high photocarrier concentration due to the bandgap shrinkage effect [25], leading to a measurable increase in the RI, which has been evaluated in detail previously [24]. As a result, the optical path difference (OPD) in the MZI increases, leading to a redshift in the interference spectrum.

The fabrication process, as shown in Fig. 2, involves the following 5 steps: (1) the side of SMF is polished in the x direction,

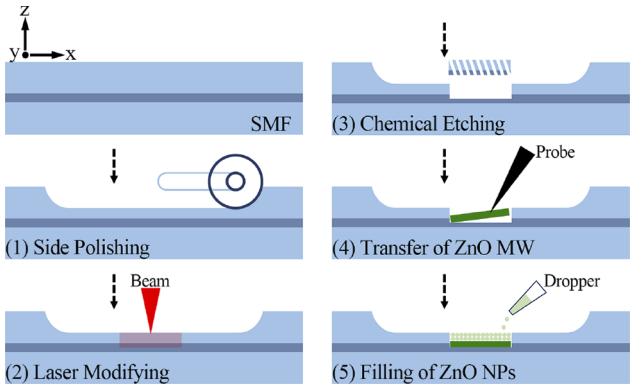

Fig. 2. Flowchart of device fabrication: (1) side polishing of SMF into D-shape with a length of 5 mm; (2) modifying a cubic area from the polished region by femtosecond laser; (3) HF etching of the modified part to create a microgroove; (4) ZnO MW transfer to the microgroove; and (5) ZnO NPs filling into the microgroove.

with a length of 5 mm and a depth of 45 μm. The residual thickness of the cladding above the core is about 20 μm. (2) The pulses emitted by the femtosecond laser processing (513 nm, 1 mW, 200 kHz) are focused through a microscopic objective (MO, $NA = 1.31$) to modify the designated area (cubic dimensions of xyz: $96 \times 3 \times 10$ μm, with the bottom reaching exactly halfway to the fiber core) of the fiber. The cubic area is formed by laser scanning line by line along the y direction to create a plane, and then layer by layer along the z direction to create a space, with a rate of 10 μm/s and a spacing of 0.5 μm between laser paths. (3) The modified area is etched with hydrofluoric acid (HF, 5%) for 60 min, and its etching rate is much higher than the other parts of the fiber. The sample is connected to a broadband light source (BBS, 1250–1650 nm) and an optical spectrum analyzer (OSA, 600–1700 nm) for real-time monitoring during etching. (4) ZnO MW (length 99.8 μm, average diameter 4.4 μm) is prepared by focus-ion-beam milling, and then it is embedded into the microgroove by tungsten probe. (5) To increase the stability of the device, the ZnO NPs (average diameter 20 nm, purity 99.9%) are filled into the microgroove.

The ZnO MWs used in this work are synthesized by chemical vapor deposition [26]. The morphology of the ZnO MW after focus-ion-beam milling is characterized by scanning electron microscope (SEM), as depicted in Fig. 3(a). The top-left inset shows ZnO NPs, and the bottom-right one depicts the end-face of ZnO MW. X-ray diffraction analysis of ZnO MW is shown in Fig. 3(b). Its crystal phase demonstrates conformity with the standard diffraction pattern of the ZnO crystal card, further

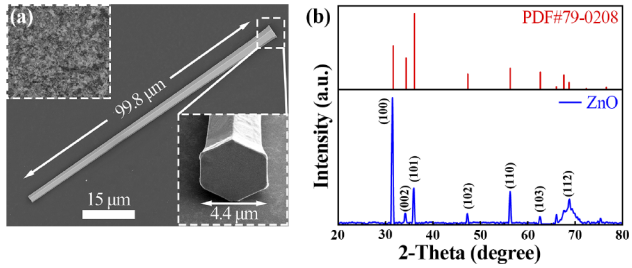

Fig. 3. (a) SEM image of the ZnO MW. The top-left and bottom-right insets show ZnO NPs and end-face of MW, respectively. (b) XRD pattern of the ZnO MW.

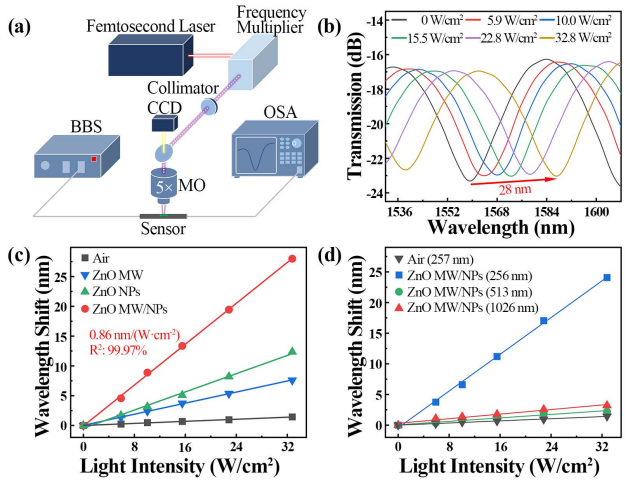

Fig. 4. (a) Experimental setup for sensitivity test of the fiber-optic UV sensor. (b) Interference spectrum drift of **ZnO MW/NPs** fiber-optic UV sensor irradiated by 257-nm laser. Wavelength shift versus light intensity in the case of ***Air*** (black), ***ZnO MW*** (blue), ***ZnO NPs*** (green), and ***ZnO MW/NPs*** (red). (d) Wavelength shift versus light intensity of *case* ***Air*** and *case* ***ZnO MW/NPs*** under different wavelength light irradiations.

confirming the successful synthesis of high-quality hexagonal ZnO MW.

Fig. 4(a) depicts the experimental setup of UV sensing for the proposed device. One end of the sensor is connected to a BBS, while the other end is connected to an OSA to monitor the interference spectrum in real time. The 200–kHz 257-nm femtosecond UV pulses, generated from the frequency quadrupling of 1026-nm femtosecond laser pulses (pulse duration of 290 fs) via a frequency multiplier, are focused onto the sensor through a MO ($NA = 0.20$). The high-repetition rate UV pulses can be roughly considered as a quasi-continuous pump. The UV sensitivity for four cases in the microgroove of the proposed sensor are investigated and denoted, respectively, as *case* ***Air*** for the non-transferred microgroove, *case* ***ZnO MW*** for fhe ZnO MW-transferred microgroove, *case* ***ZnO NPs*** for the ZnO NPs-transferred microgroove, and *case* ***ZnO MW/NPs*** for the ZnO MW and NPs-transferred microgroove, for simplicity.

With the increase of UV intensity from 0 to 32.8 W/cm^2, the interference wavelength shows an evident redshift of about 28 nm for the proposed fiber-optic UV sensor (namely, in *case* ***ZnO MW/NPs***), as can be seen in Fig. 4(b). For comparison, the wavelength shift and UV sensitivity for all cases in the microgroove (namely, ***Air***, ***ZnO MW***, ***ZnO NPs***, and ***ZnO MW/NPs***) of the proposed device are plotted in Fig. 4(c). In *case* ***Air***, the OPD of the proposed device is possibly increased by the photothermal effect only, which originates from the slight UV absorption of the SMF material and leads to a small redshift of 1.4 nm in the interference wavelength. In *case* ***ZnO MW***, the total wavelength shift is 7.6 nm, which is much higher than that of *case* ***Air***. This indicates that the OPD increase is mainly caused by the photocarriers induced RI change in ZnO MW, which has overcome the opposite contribution of the photothermal effect in the remaining fiber core. This competitive advantage is more evident in *case* ***ZnO NPs***, where NPs with large specific surface areas are beneficial for sufficient UV absorption and the total wavelength shift achieves 12.6 nm. However, the ZnO NPs also bring a large insertion loss due to significant scattering. In *case* ***ZnO MW/NPs***, the implementation of ZnO NPs considerably reduces the air gap between the ZnO NW and the microgroove and substantially increases the UV absorption of the sensing area compared to that of *case* ***ZnO MW***. Hence, the total wavelength shift is notably increased to 28 nm, corresponding to a UV sensitivity of 0.86 nm/(W·cm^{-2}) through linear fitting, which is 3.7 times that of *case* ***ZnO MW***.

To verify the wavelength selectivity of the proposed UV sensor, the **ZnO MW/NPs** sample undergoes irradiation of the visible (513 nm) and near-infrared (1026 nm) femtosecond laser beams, respectively. The relationship between the wavelength threshold ($\lambda_{(nm)}$) of light absorption and semiconductor's bandgap (E_g in eV) can be described as follows [27]:

$$\lambda_{(nm)} = 1240/E_g. \tag{2}$$

According to Eq. (2), the ZnO material experiences intrinsic absorption and exhibits changes in the carrier concentration when irradiated by UV with a wavelength shorter than 368 nm. Thus, it can be considered that the interference wavelength shift of the device is induced by the photothermal effect only, due to the non-absorption of ZnO in visible and near-infrared bands. Note that the photothermal effect will result in a temperature increase of the ZnO material, of which the thermal-optic coefficient is 2.31×10^{-4} /K [28]. This means that the RI of ZnO material increases with temperature increasing, which will lead to a redshift of the interference wavelength. From Fig. 4(d), it can be observed that the interference wavelength experiences a redshift of 2.2 nm and 3.2 nm, as the 513-nm and 1026-nm light intensity increases, respectively, implying a more significant photothermal effect under the excitation of the near-infrared. The results of *case* ***Air*** and *case* ***ZnO MW/NPs*** under 257-nm UV illumination are also presented in Fig. 4(d) for comparison, where it can be found that the wavelength shift resulting from 513-nm and 1026-nm illumination can be ignored. Consequently, the proposed sensor indeed exhibits UV wavelength selectivity and negligible photothermal effect.

Response time of the proposed UV sensor is also investigated by the experimental setup shown in Fig. 5(a), where nanosecond UV pulses delivered from a Nd:YAG laser (λ=266 nm, repetition

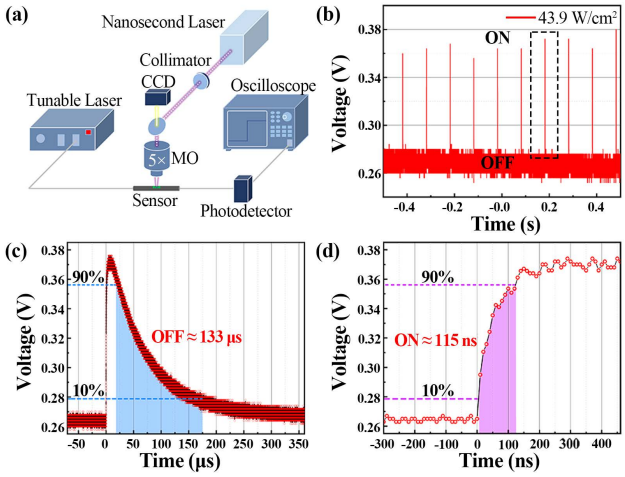

Fig. 5. (a) Experimental setup for the temporal response test of the fiber-optic UV sensor. (b) Continuous pulse response under 10-Hz, 266-nm, 7-ns pulsed UV laser. (c) Magnification of the time response of a single pulse. (d) Further magnification of the rising edge in (c).

Table 1. Performance Comparison of Various UV Detectors Based on ZnO Materials

UV detector	λ	Responsivity / Sensitivity	t_{on} / t_{off}	Ref.
ZnO/Cu_2O	355 nm	19.3 mA/W	0.14 s / 0.36 s	[30]
ZnO/Ni	350 nm	7.52 μA/W	0.5 s / 2 s	[31]
ZnO/Ag	365 nm	14.43 A/W	9.37 s / 6.91 s	[32]
ZnO/Co	365 nm	8.76 A/W	0.229 s / 0.276 s	[33]
ZnO nanowire	266 nm	1.66 nm/($W \cdot cm^{-2}$)	0.43 ms / 0.47 ms	[22]
ZnO microwire	266 nm	0.29 nm/($W \cdot cm^{-2}$)	0.56 ms / 0.7 ms	[26]
ZnO MW/NPs	257 nm	0.86 nm/($W \cdot cm^{-2}$)	115 ns / 133 μs	This work

rate 10 Hz, and pulse duration 7 ns) are focused onto the sample through a lens. According to the edge filtering method [29], a tunable laser, a photodetector, and an oscilloscope are used to record the temporal response of the sample. Fig. 5(b) depicts the temporal response of the sample to 10 laser pulses within 1 s, demonstrating its good stability and rapid response. Here we define the response time to be the duration taken by a signal to change from 10% to 90% between its low and high levels, and vice versa. Fig. 5(c) shows the magnification of a single-pulse response, and further magnification of its rising edge is shown in Fig. 5(d). According to the curves of the rising and decaying edges, the rise time and decay time are estimated to be 115 ns and 133 μs, respectively. In comparison with the previously reported electric-based [30–33] and optical fiber-based UV photodetectors [22,26,34], the device proposed here exhibits faster response speed, as listed in Table 1. The primary reason lies on the fact that the proposed device employing the transient RI change induced by the generation of photocarriers and is independent of photocarrier diffusion and migration in the bulk ZnO material, which essentially results in an improvement in device response time. The main reasons for the slow decay time may be the existence of trapped holes with extended lifetimes, which may originate from defects in the ZnO crystals or surface damage during device processing. Furthermore, the adsorption of oxygen on ZnO surfaces may also prolong the decay time [35,36].

In this work, a ZnO microwire-based single-fiber Mach–Zehnder interferometer is demonstrated for UV sensing, where a ZnO microwire and the remaining fiber core act as the sensing arm and the reference arm, respectively. The ZnO microwire is embedded in a microgroove that reaches half of the fiber core, which is fabricated through processes of side polishing, femtosecond laser micromachining, and chemical etching. Experimental results indicate that the device achieves a UV sensitivity of up to 0.86 nm/($W \cdot cm^{-2}$) under 257-nm laser pulse irradiation. The rise time and decay time are measured to be 115 ns and 133 μs, respectively, by utilizing 266-nm and 5-ns laser pulse excitation. The high sensitivity and fast response of the proposed sensor are beneficial to the development of future high-performance UV sensors.

Funding. National Key Research and Development Program of China (2022YFE0111400); Natural Science Foundation of Guangdong Province (2023A1515012893); Shenzhen Key Laboratory of Ultrafast Laser Micro/Nano Manufacturing (ZDSYS20220606100405013); Science and Technology Innovation Commission of Shenzhen (JCYJ20200109114001806, JCYJ20220818095615034).

Disclosures. The authors declare no conflicts of interest.

Data availability. Data underlying the results presented in this paper are not publicly available at this time but may be obtained from the authors upon reasonable request.

REFERENCES

1. P. Vashishtha, L. Goswami, S. K. Jain, *et al.*, J. Alloys Compd. **930**, 167267 (2023).
2. S. Knobelspies, A. Daus, G. Cantarella, *et al.*, Adv. Electron. Mater. **2**, 1600273 (2016).
3. W. Tian, H. Lu, and L. Li, Nano Res. **8**, 382 (2015).
4. Q. Wang, Y. Zhang, X. Wangjin, *et al.*, J. Environ. Sci. **87**, 272 (2020).
5. C. L. Joseph, Exp. Astron. **6**, 97 (1995).
6. W. Zheng, L. Jia, and F. Huang, iScience **23**, 101145 (2020).
7. B. López Paredes, H. Araújo, F. Froborg, *et al.*, Astroparticle Physics **102**, 56 (2018).
8. M. Richter, A. Gottwald, U. Kroth, *et al.*, Appl. Phys. Lett. **83**, 2970 (2003).
9. A. Rogalski, Z. Bielecki, and J. Wojtas, Sensors **23**, 4452 (2023).
10. B. Culshaw, J. Lightwave Technol. **22**, 39 (2004).
11. T. Toda, M. Hata, Y. Nomura, *et al.*, Jpn. J. Appl. Phys. **43**, L27 (2004).
12. D. Li, K. Jiang, X. Sun, *et al.*, Adv. Opt. Photonics **10**, 43 (2018).
13. D. Kaur and M. Kumar, Adv. Opt. Mater. **9**, 2002160 (2021).
14. D. Gedamu, I. Paulowicz, S. Kaps, *et al.*, Adv. Mater. **26**, 1541 (2014).
15. Y. Yan, X. Zhang, H. Li, *et al.*, Sensors **18**, 3754 (2018).
16. Z. Helil, R. Jamal, M. Niyaz, *et al.*, Pol. J. Chem. Technol. **24**, 7 (2022).
17. Y. Chen, D. Bagnall, and T. Yao, Mater. Sci. Eng., B **75**, 190 (2000).
18. C. Soci, A. Zhang, B. Xiang, *et al.*, Nano Lett. **7**, 1003 (2007).
19. H. Kind, H. Yan, B. Messer, *et al.*, Adv. Mater. **14**, 158 (2002).
20. W. Ouyang, J. Chen, and X. Fang, Appl. Phys. Rev. **8**, 031315 (2021).
21. Y. Ning, Z. Zhang, F. Teng, *et al.*, Small **14**, 1703754 (2018).
22. L. Zhang, Y. Wang, H. Wu, *et al.*, Nanoscale **11**, 8319 (2019).
23. T. Shen, X. Dai, D. Zhang, *et al.*, Sensors **20**, 1478 (2020).
24. B. Bennett, R. Soref, and J. Del Alamo, IEEE J. Quantum Electron. **26**, 113 (1990).
25. A. P. Roth, J. B. Webb, and D. F. Williams, Phys. Rev. B **25**, 7836 (1982).
26. H. Wu, Y. Wang, L. Zhang, *et al.*, J. Lightwave Technol. **39**, 4225 (2021).
27. F. Wooten and S. P. Davis, Am. J. Phys. **41**, 939 (1973).
28. A. Kaphle, E. Echeverria, D. N. McIlroy, *et al.*, J. Nanosci. Nanotechnol. **19**, 3893 (2019).
29. C. Liao, D. Wang, Y. Li, *et al.*, Appl. Opt. **48**, 3001 (2009).
30. Z. Bai and Y. Zhang, J. Alloys Compd. **675**, 325 (2016).
31. F. Abbasi, F. Zahedi, and M. H. Yousefi, Opt. Commun. **482**, 126565 (2021).
32. B. Hanna, L. R. Pillai, K. Rajeev, *et al.*, Sens. Actuators, A **338**, 113495 (2022).
33. R. Shabannia, Mater. Lett. **214**, 254 (2018).
34. D. Ma, Y. Wang, C. Chen, *et al.*, Opt. Express **31**, 5102 (2023).
35. Y. Liu, C. R. Gorla, S. Liang, *et al.*, J. Electron. Mater. **29**, 69 (2000).
36. M. H. Mamat, M. Z. Sahdan, S. Amizam, *et al.*, AIP Conf. Proc. **1136**, 591 (2009).